

# Low-End Mass Function of the Arches Cluster

Jihye Shin<sup>1,2\*</sup> and Sungsoo S. Kim<sup>2,3†</sup>

<sup>1</sup>*Kavli Institute for Astronomy and Astrophysics at Peking University, Yi He Yuan Lu 5, Hai Dian District, Beijing 100871, P.R. China*

<sup>2</sup>*School of Space Research, Kyung Hee University, Yongin, Kyungki 446-701, Republic of Korea*

<sup>3</sup>*Department of Astronomy & Space Science, Kyung Hee University, Yongin, Kyungki 446-701, Republic of Korea*

Accepted 2014 November 12. Received 2014 November 11; in original form 2014 October 5

## ABSTRACT

The initial mass function (IMF) of the Arches cluster, which was formed a few million years ago in the harsh environment of the Galactic center (GC), has long been a target of interest to those who study the GC and the theory of star formation. The distinct star-forming conditions in the GC might have caused the cluster to have a shallower slope or an elevated lower mass cutoff in its IMF. But its mass function has been revealed only down to  $1\text{--}2 M_{\odot}$  (the lower limit of resolved stars), and the low-end mass function of the Arches is still unknown. To estimate the unresolved part of the Arches mass function, we have devised a novel photometric method that involves the histogram of pixel intensities in the observed image, which contains information on the unresolved, faint stars. By comparing the pixel intensity histograms (PIHs) of numerous artificial images constructed from model IMFs with the observed PIH, we find that the best-fit model IMF for the Arches cluster has a cutoff mass less than or similar to  $0.1 M_{\odot}$  and a shape very close to that of the Kroupa MF. Our findings imply that the IMF of the Arches cluster is similar to those found in the Galactic disk.

**Key words:** techniques: photometric – Galaxy: centre – galaxies: star clusters – stars: formation.

## 1 INTRODUCTION

The Arches cluster is a young (2–4 Myr), compact ( $\leq 1$  pc), and massive ( $\sim 2 \times 10^4 M_{\odot}$ ) star cluster located 26 pc away from the Galactic center (GC) in projection (Figer et al. 1999; Kim et al. 2000; Figer et al. 2002; Najarro et al. 2004; Martins et al. 2008; Espinoza, Selman & Melnick 2009). This extraordinary cluster has been suspected to have had a shallower initial mass function (IMF) or an elevated low-mass cutoff ( $M_l$ ) in the IMF, compared to the IMFs inferred for the Galactic disk clusters because of the extreme environment of the GC, such as elevated temperatures and turbulent velocities in the molecular clouds, strong magnetic fields, and large tidal forces (Morris 1993). The Quintuplet cluster is another young (3–5 Myr), massive ( $\sim 10^4 M_{\odot}$ ) cluster in the GC area (Figer et al. 1999), but it is much less dense in number density than the Arches, and thus it is more difficult to estimate its mass function from the photometry because of the confusion problem with the foreground and background stars. The Arches cluster is an excellent target for understanding the effects of the star-forming environment on the IMFs of star clusters.

The first high-resolution photometry toward the Arches

was performed by Figer et al. (1999) using the infrared (IR) camera onboard the *Hubble Space Telescope* (HST). They estimated the cluster’s mass function (MF) down to  $\sim 6 M_{\odot}$ , which was the mass corresponding to the 50% completeness limit of their photometry,  $M_{50}$ . This has been followed by several adaptive optics (AO) IR observations with a few ground telescopes. Stolte et al. (2002) obtained  $M_{50} = 5.6 M_{\odot}$  with the Gemini telescope, and Stolte et al. (2005) acquired  $M_{50} = 2.3 M_{\odot}$  with the Very Large Telescope (VLT). Kim et al. (2006) obtained the lowest  $M_{50}$  so far,  $1.3 M_{\odot}$ , with the Keck telescope. The IMF estimated in Kim et al. was only slightly shallower (power-law exponent of  $\Gamma = -1.0$  to  $-1.1$ ) than the Salpeter IMF (Salpeter 1955;  $\Gamma = -1.35$ ), and it did not indicate an elevated low-mass cutoff, at least not down to  $1.3 M_{\odot}$ .

Resolving stars fainter than  $1.3 M_{\odot}$  in the Arches cluster will have to wait until the next-generation IR space telescope, such as the *James Webb Space Telescope*, or an extremely large ground telescope, such as the Giant Magellan Telescope, is available. In the present paper, we devise a method to estimate the shape of the low-end MF, where the individual stars are not resolved, and apply it to the Arches cluster.

In a conventional photometric method, stars in the observed image are identified by fitting the point spread function (PSF). However, our goal here is to estimate the number

\* Email: jhshin.jhshin@gmail.com

† Corresponding author

distribution of stars fainter than the photometric completeness limit (i.e., the stars that are too faint to be fit with the PSF). Our new method involves the histogram of pixel intensities in the observed image.

In most star clusters, faint stars are more abundant than bright ones. If the number of unresolved stars is large enough, they will have a non-negligible contribution to the pixel intensities and the number distribution of pixel intensities in the observed image. Thus, the pixel intensity histogram (PIH) of an observed image can give valuable information about unresolved, faint stars. With our method, we estimate the MF of the Arches cluster below the photometric completeness limit by fitting the PIHs of model images to the observed PIH.

We first build a synthetic luminosity function (LF) for the cluster by combining the observed LF above the magnitude of the completeness limit (limiting magnitude) and a model LF, which is converted from a model MF below the limiting magnitude. We also build a synthetic LF for the fore/background stellar population toward the Arches cluster using the Milky Way star-count model of Wainscoat et al. (1992). We then create an artificial image from these two synthetic LFs and compare the PIH of this image to the observed PIH. We try various model LFs below the limiting magnitude until we find satisfactory agreement between the synthetic and observed PIHs.

Our new method does not directly yield an LF or MF of a cluster. However, it can be used to reject certain MFs, and we find that the IMF of the Arches cluster should not be too different from that for the Galactic disk, such as the Kroupa IMF (Kroupa 2001).

This paper is organized as follows. In §2, we describe the observational data and the photometric procedures used in the present study. We discuss the fore/background stellar population toward the Arches cluster and the background flux in the observed images in §3. §4 describes the procedures to search for the most plausible MF of the Arches cluster. Summary and conclusion are given in §5.

## 2 OBSERVATIONAL DATA AND PHOTOMETRY

The imaging data of the Arches cluster that we use in this study were obtained with the NICMOS2 camera onboard the *HST* on UT September 13/14, 1997 (Figer et al. 1999). We chose this data set among others not only because the PSFs of space observations are relatively stable and well known, but also because this data set includes the images of control fields near the target cluster. The NICMOS2 camera has a field-of-view (FOV) of  $19''.2 \times 19''.2$  and  $256 \times 256$  pixels (each pixel covers  $0''.076 \times 0''.076$  of the sky). The Arches cluster was observed in a mosaic-pattern of  $2 \times 2$ , and three control fields were observed at a distance of  $60''$  from the center of the cluster field (Fig. 1). All image data were taken with F110W, F160W, and F205W filters, but the present study makes use of only F205W images because they suffer the smallest extinction. The exposure time of all F205W images used in the present study is 256 s.

Data were reduced using STScI pipeline routines, and PSF photometry (star-finding, PSF-building, and PSF-fitting) was performed using the DAOFIND and DAOPHOT

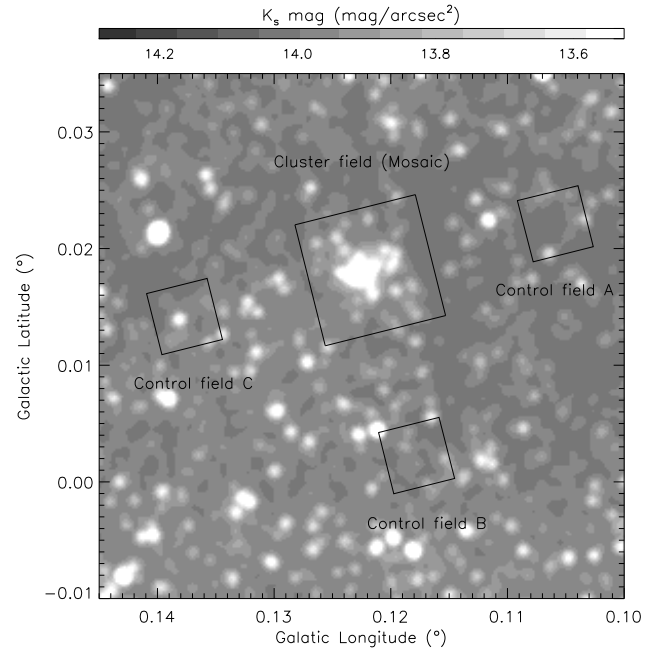


**Figure 1.** Locations and image sizes of the cluster field and the three control fields used in the present study. All fields were observed by the NICMOS2 camera onboard the *HST* (Figer et al. 1999). The cluster field was observed in a  $2 \times 2$  mosaic pattern. The background, a  $K_s$ -band image from the 2MASS (Skrutskie et al. 2006), is to show that the three control fields have fairly uniform background emission levels.

packages (Stetson et al. 1987) within the Image Reduction and Analysis Facility (IRAF).<sup>1</sup> The conversion of the PSF flux into the Vega magnitude was done using the photometric keywords and zero-points announced on the STScI webpage<sup>2</sup>.

The photometry of faint stars is incomplete due to their low signals and confusion by nearby brighter stars. We estimated recovery fractions for each 0.5 magnitude bin by planting artificial stars on the images. The obtained LFs were corrected using the recovery fractions. In our analyses in the forthcoming sections, only the portion of LF whose recovery fraction is higher than 50% is used.

We adopted a distance modulus of 14.52 for the GC ( $R_g = 8$  kpc; Reid 1993) and solar-metallicity isochrone at 2 Myr of the Geneva model (Lejeune & Scharer 2001) for the conversion between the stellar magnitude and the mass. The reddening value of each star was estimated from the color excess in F160W–F205W color and the extinction law of Rieke, Rieke & Paul (1989). The average extinction estimated for the cluster was 2.9 mag in F205W.

<sup>1</sup> IRAF is distributed by the National Optical Astronomy Observatories, which are operated by the Association of Universities for Research in Astronomy, Inc., under cooperative agreement with the National Science Foundation.

<sup>2</sup> <http://www.stsci.edu/hst/nicmos/performance/photometry>

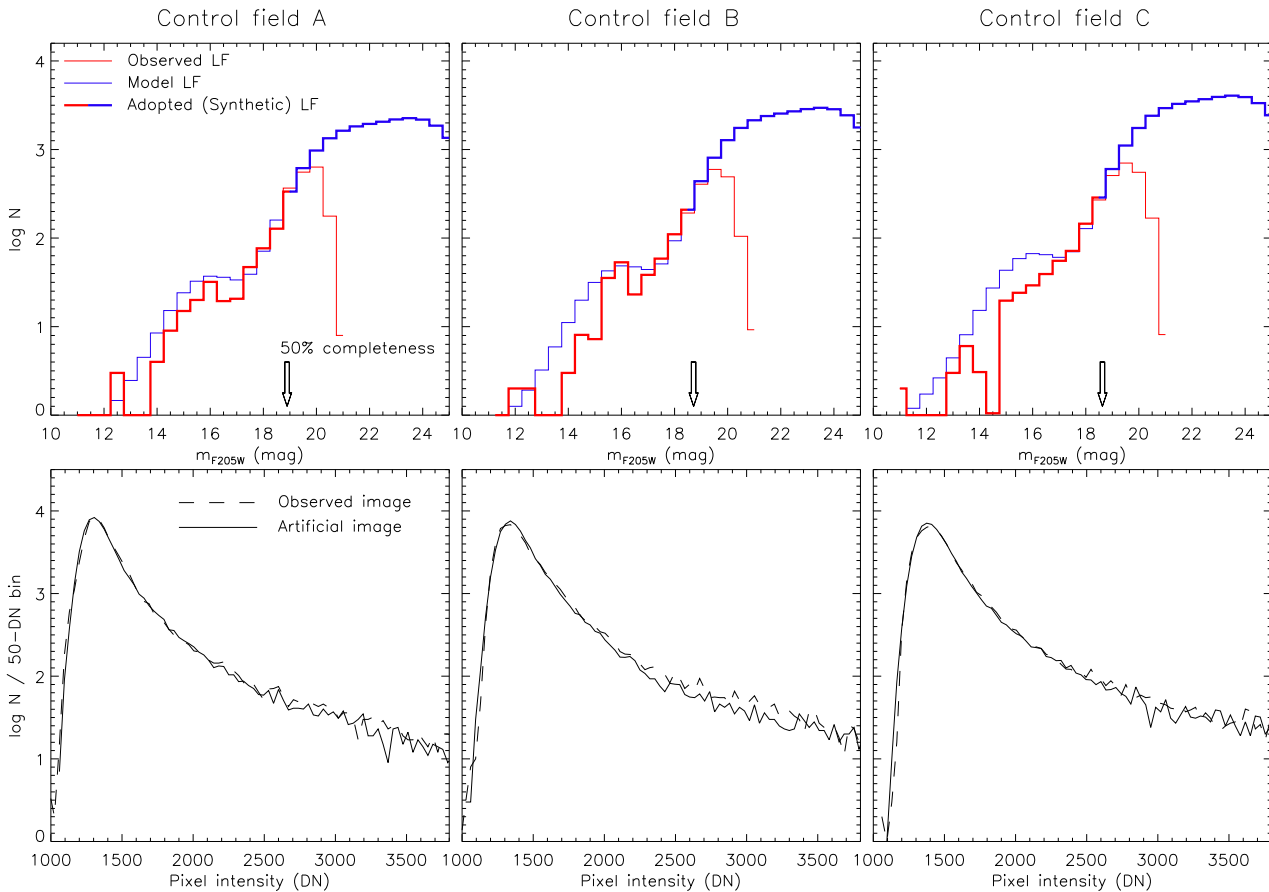


**Figure 2.** Luminosity functions (LFs) and pixel intensity histograms (PIHs) of the control fields A, B, and C (left, middle, and right panels). In the upper panels, the red lines are completeness-corrected LFs from the observations, and the blue lines are the model LFs from the star-count model of Wainscoat et al. (1992). We vertically shifted the model LFs to match them with the observed LFs at  $m_{50}$  (arrows), then built the synthetic LFs (thick lines) by combining the observed LFs for the bright-part and the model LFs for the faint-part. The lower panels compare the observed PIHs with the PIHs of the artificial images constructed from the corresponding synthetic LFs (solid lines). The histograms are the number of pixels for each 50-DN bin.

## 2.1 The Control Fields

Before constructing the fore/background LF toward the Arches cluster, we first constructed the synthetic LFs in each direction of the three control fields. For the magnitude bins brighter than the magnitude of 50% completeness,  $m_{50}$ , of each field (18.9, 18.7, and 18.6 mag for control fields A, B, and C, respectively), we adopted the completeness-corrected F205W LFs from each field. For the magnitude bins fainter than  $m_{50}$ , we constructed model LFs by integrating the model number density of stellar objects within a given apparent K-mag range along the pencil-beam volume element in the direction of each control field. For the model number density, we used the star-count model of the Milky Way in the K band by Wainscoat et al. (1992), which considers 87 different stellar types and various Galactic structures such as the disk, bulge, halo, and spiral arms (here we assumed that the LFs in the K and F205W bands are adequately similar). The K magnitudes of stellar objects in the star-count model are reddened with an average extinction of 2.9 mag and observed standard deviations of 2.1, 1.6, and 1.8 mag for control fields A, B, and C, respectively.

Ideally, the bright-part LF from the PSF photometry

and the faint-part LF from the star-count model should connect smoothly at  $m_{50}$ . However, the faint-part logarithmic LFs were found to be  $\sim 0.25$  dex higher than the bright-part log LFs at  $m_{50}$ . This is thought to be because the star-count model by Wainscoat et al. (1992) is not accurate enough, particularly toward the GC region, due to the large amounts of extinction. For this reason, we subtracted 0.31, 0.28, and 0.19 dex from the model log LFs of control fields A, B, and C, respectively, so the model LFs at  $m_{50}$  match with the observed LFs. Then we constructed the final synthetic LF by merging the bright-part LF from the PSF photometry and the modified faint-part LF from the star-count model.

The upper panels of Figure 2 show the completeness-corrected LFs from observations (red lines), the model LFs modified (shifted vertically as described above) to match the observed LFs at  $m_{50}$  (blue lines), and the final synthetic LFs for the three control fields (thick lines).

We then constructed the artificial images using these synthetic LFs for each control field. For this, we first built a set of 64 model PSFs at  $8 \times 8$  equally-spaced grid points

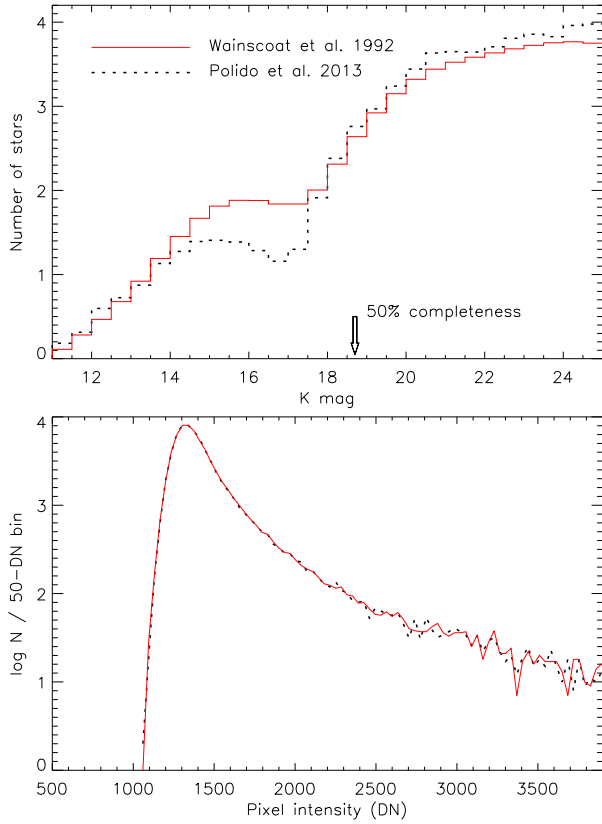


**Figure 3.** (Upper panel) Model LFs toward the Arches cluster region by Wainscoat et al. (1992) and by Polido, Jablonski, & Lépine (2013). The arrow marks the magnitude of 50% completeness,  $m_{50}$ . (Lower panel) PIHs of the artificial images for the control field A that are constructed with the star-count models by Wainscoat et al. (1992) and by Polido, Jablonski, & Lépine (2013). For the latter, the model log LF was vertically shifted downward by 0.34 dex in order to match it with the observed LF at  $m_{50}$ .

of the detector plane using the Tiny Tim,<sup>3</sup> a PSF modelling tool. Each model PSF has  $80 \times 80$  pixels. Then we planted artificial stars at random locations in the artificial images, using whichever of the 64 model PSFs was closest to the location of the artificial star being planted. The magnitude of the artificial star was chosen randomly following the synthetic LF for each control field. A dark current of  $76.8 e^-$  and readout noise with a standard deviation of  $\sqrt{26} e^-$  were added to the artificial images. Poisson uncertainties and a gain of  $5.4 e^-/\text{DN}$  [conversion between the electrons and the data number (DN)] were considered when adding the artificial stars, dark current, and background flux (discussed below).

The final artificial image was completed by adding a proper background flux, which is rather difficult to estimate theoretically. The background flux includes telescopic thermal noise, zodiacal light, external galactic sources, and cosmic IR background. The instrument handbook of the NICMOS camera predicts that thermal noise is the dominant background source, with an estimated flux of  $\sim 550$  DN

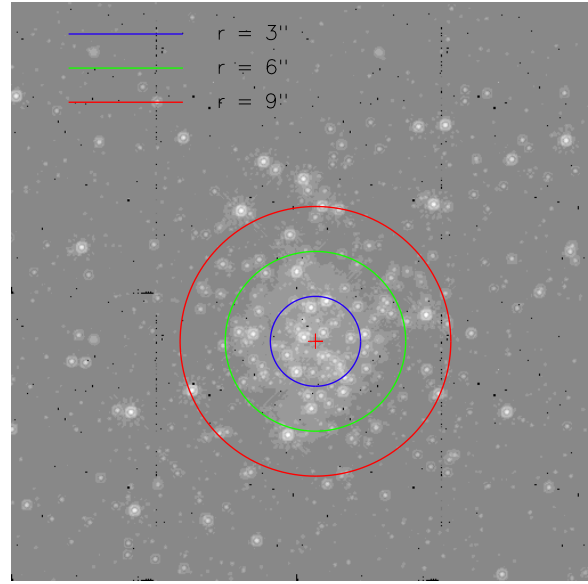


**Figure 4.** Cluster field image obtained with a F205W filter and the three annuli of 3, 6, and 9'' (corresponding to 0.12, 0.23, and 0.35 pc) from the cluster center, which is marked with the cross.

for an exposure of 256 s. However, the flux level from the thermal noise can vary over time, and the exact amount of background flux from the zodiacal light and cosmic IR background in the F205W band is not well known either.

Perhaps using the observed PIHs themselves is the best way to estimate the background flux. The lower panels of Figure 2 show the faint ends (DN smaller than 3,800) of the PIHs. These faint-end PIHs correspond to pixels that do not belong to the main body of any bright, resolved stars (the peak DN of a star with  $m_{50}$  is  $\sim 3500$ ). The intensities in this part of a PIH are mostly from various background sources and faint, unresolved stars. We found that adding a background flux of 1,190 DN resulted in a good match between the PIHs from observed and artificial images for all three control fields.

This demonstrates that we are able to reproduce the observed PIHs in the directions of the three control fields with our procedures for constructing the fore/background stellar LF and artificial images, and that we are now ready to apply our procedures to the Arches cluster to reveal the faint-part LF of the cluster itself. The background flux of 1,190 DN obtained for the control fields will be used for the cluster field in §4 as well.

The faint-end PIHs of our artificial images for the control fields are statistically stable against the random choices of magnitudes and positions for the artificial stars because the number of pixels with  $\text{DN} \lesssim 3,000$  in the artificial images (and thus in the observed images as well) is large enough ( $\sim 50 \sim 10,000$  for the 50-DN bin).

To check if the PIHs of our artificial images are dependent on the choice of the star-count model for the faint-part LF, we have also tried the star-count model by Polido, Jablonski, & Lépine (2013), which is a modified version of the model by Ortiz & Lépine (1993). The upper panel of Figure 3 compares the model LFs toward the Arches cluster region by Wainscoat et al. (1992) and by Polido, Jablonski, & Lépine (2013). The shapes of the two

<sup>3</sup> <http://www.stsci.edu/hst/observatory/focus/TinyTim>

LFs are quite similar at the faint-part (below  $m_{50}$ ). Although the LF by Polido et al. is slightly higher at the magnitudes below  $m_{50}$ , this does not matter much because we vertically shift the model LF anyway to match it with the observed LF at  $m_{50}$ . The lower panel of Figure 3 compares the PIHs of the artificial images for the control field A that are constructed with the two star-count models, and the two PIHs are nearly indistinguishable. This shows that our procedure of constructing the artificial images for fore/background stars is robust against the choice of star-count model for the faint-part LF.

### 3 THE CLUSTER FIELD

Unlike in the control fields, in the cluster field the stellar number density and LF are highly position-dependent. At the center of the cluster, confusion by bright stars is so significant that the contribution of the faint cluster stars to the PIH is almost negligible. On the outskirts of the cluster, the photometry is limited by the fore/background stars and the contribution of faint cluster stars to the PIH becomes insignificant relative to the fore/background stars. Thus the best region for a study of faint cluster stars is the intermediate region between the cluster center and the outskirts. We chose two annuli ( $3'' < r < 6''$  and  $6'' < r < 9''$ ) for our analyses here. [Fig. 4; we adopted the position of the cluster center used in Figer et al. (1999); note that Kim et al. (2000) estimates the tidal radius of the cluster to be  $\sim 26''$ ].

Our stellar photometry and completeness test resulted in  $m_{50} = 16.0$  mag for  $3'' < r < 6''$  and 17.4 mag for  $6'' < r < 9''$ . As in the control fields, our synthetic LFs for the two cluster annuli are composed of two parts: the bright-part LF from our PSF photometry for magnitude bins brighter than  $m_{50}$  and the faint-part LF from a model for magnitude bins fainter than  $m_{50}$ .

The faint-part model LF consists of 1) the model LF for the fore/background stars and 2) the LF converted from a model MF for the cluster stars. For the fore/background model LF, we used the average of the three synthetic LFs for the control fields. For the cluster model LF, we tried the following two models: 1) LFs converted from single power-law MFs with various exponents and lower mass limits, and 2) LFs converted from the Kroupa MF (Kroupa 2001) with various lower mass limits.

We constructed artificial images for the two cluster annuli following the same procedure used for the control fields. However, the area covered by each cluster annulus is rather small, and we found that the shape of the faint-end PIH depended slightly on the random choices of magnitudes and positions of bright artificial stars. Therefore, we used the magnitudes and positions of the actual, observed stars when planting artificial stars brighter than  $m_{50}$  instead of randomly selecting their magnitudes and positions from the observed LF.

A background flux of 1,190 DN was applied to the artificial images for the cluster annuli, which is the value deduced from the control field images.

#### 3.1 Single Power-Law Mass Function

In this subsection, we describe our attempts with the single power-law MFs with various power-law exponents  $\alpha$  ( $dN \propto M^{-\alpha} dM$ ) and  $M_l$  for the faint-part LF of the cluster. The upper panels of Figure 5 show some sample synthetic LFs for the  $3'' < r < 6''$  annulus, whose faint-part cluster LFs are from the MFs with three different  $\alpha$  values (left panel), and three different  $M_l$  values (right panel).

The lower panels of Figure 5 plot the faint-end PIHs of the observed image (dotted lines) and those of the artificial images constructed from the synthetic LFs in the corresponding upper panels (solid lines). First, the heights of PIHs from the artificial images are generally consistent with those from the observed image, implying that our procedure of constructing artificial images for the cluster field has no fundamental flaws. Second, the turnover intensity of the PIH clearly depends on the  $\alpha$  and  $M_l$  values (though it is less sensitive on small  $\alpha$  and large  $M_l$  values). This second point demonstrates that the PIHs can be used to reject or accept assumed faint-end LFs (and thus MFs) for the Arches cluster.

The few sample experiments shown in Figure 5 already imply that the best-fit  $\alpha$  and  $M_l$  are around 2.2-2.3 and 0.1-0.3  $M_{\odot}$ , respectively. To more quantitatively search for the  $\alpha$  and  $M_l$  values that best fit the observed PIH, we devised a statistic:

$$S = \langle (\log N_{obs}(I) - \log N_{art}(I))^2 \rangle_{N>100}, \quad (1)$$

where  $N_{obs}(I)$  and  $N_{art}(I)$  are the numbers of pixels with an intensity (DN)  $I$  in the observed and artificial images, respectively. The bracket indicates an average, and we chose to average only numbers with  $N(I) > 100$ . This rather unusual statistic was adopted because the logarithmic shape of the PIH better discerns different  $\alpha$  and  $M_l$  values than the linear shape does.

The color map of  $\log S$  in the  $\alpha$ - $M_l$  space for the two cluster annuli are shown in panels a and b of Figure 5. The minimum  $\log S$  is near ( $\alpha = 2.3$ ,  $M_l = 0.2 M_{\odot}$ ) for the inner annulus and near ( $\alpha = 1.9$ ,  $M_l = 0.02 M_{\odot}$ ) for the outer annulus. The  $\log S$  contours near the minima are rather elongated along the curves connecting the (large  $\alpha$ , large  $M_l$ ) and (small  $\alpha$ , small  $M_l$ ) corners because those curves have similar contributions (roughly in numbers) of faint stars to the faint-ends of the PIHs.

The simplest way to estimate the best-fit  $\alpha$  and  $M_l$  values from the two annuli simultaneously is perhaps by adding the  $S$  values from the two annuli. The sum of the two  $S$  values has a minimum at ( $\alpha = 2.2$ ,  $M_l = 0.1 M_{\odot}$ ) and has less elongated contours around the minimum (Fig. 6c).

Our simple analyses with single power-law MFs imply that the present-day MF of the Arches is not significantly different from the Salpeter MF whether the two annuli are considered separately or simultaneously.

#### 3.2 Kroupa Mass Function

In this subsection, we use more realistic MF models for the faint-part LF of the cluster. We adopted the Kroupa MFs (Kroupa 2001) with various  $M_l$  as the initial MF of the cluster, and allowed them to dynamically evolve for 2 Myr with the anisotropic Fokker-Plank (F-P) model

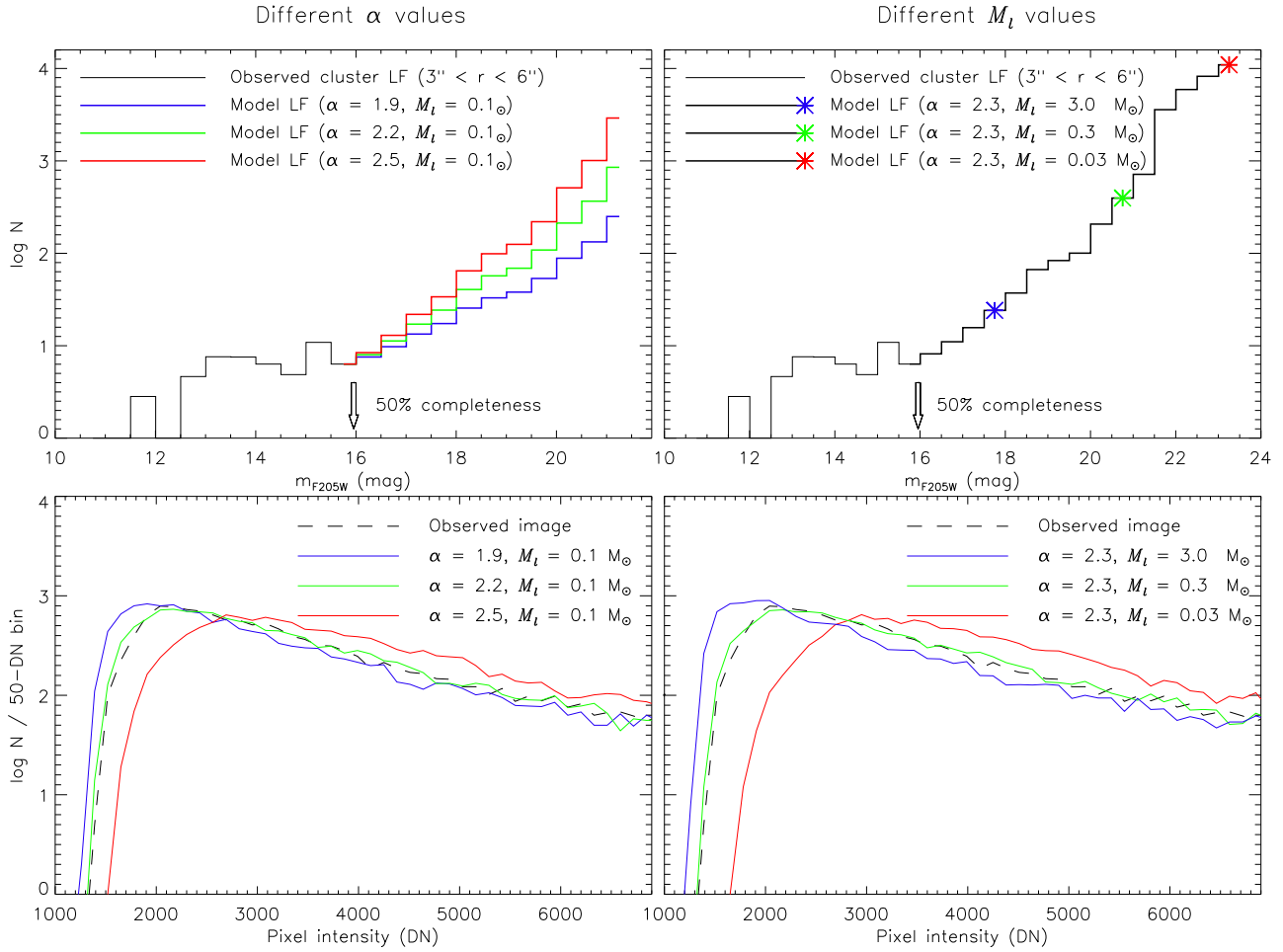


**Figure 5.** LFs and PIHs of the cluster field with different  $\alpha$  (left panels) or  $M_t$  (right panels) values for single power-law MFs. The model LFs, converted from the model MFs, are connected with the observed cluster LF at  $m_{50}$  (upper panels) to form the synthetic LFs. The PIHs of the artificial images constructed from the synthetic LFs are compared with the observed PIH (lower panels).

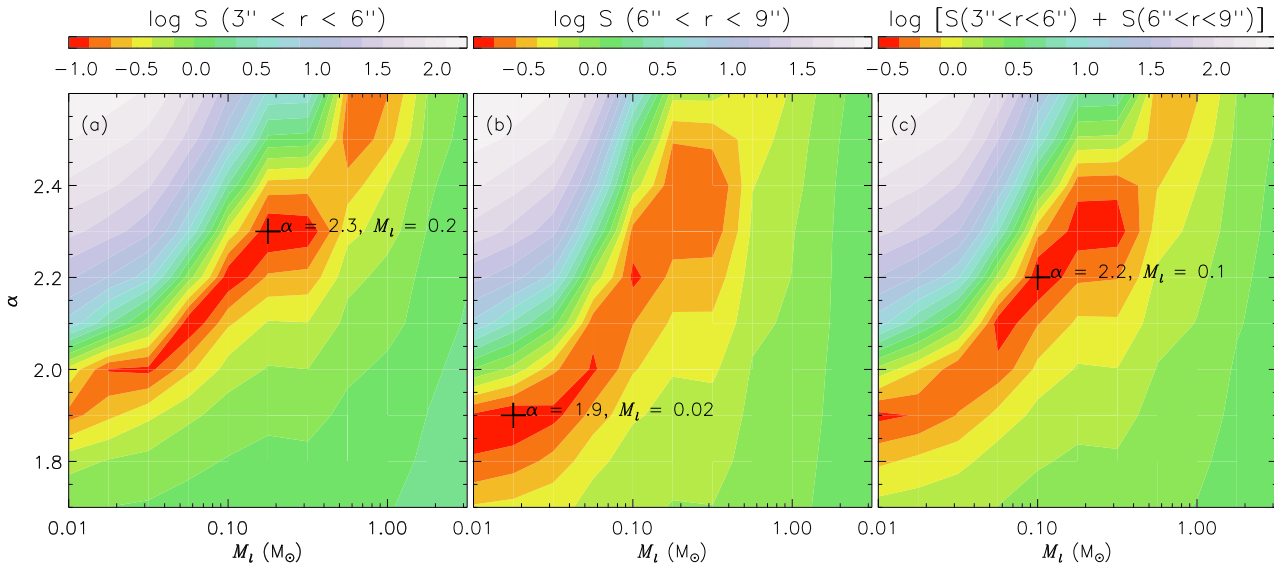


**Figure 6.** Color maps of  $\log S$  of the cluster field in  $\alpha - M_t$  space for a single power-law MF. The left and middle panels are for  $3'' < r < 6''$  and  $6'' < r < 9''$  annuli, respectively, and the right panel is for the two annuli together. The minimum  $\log S$  points are marked with cross symbols.

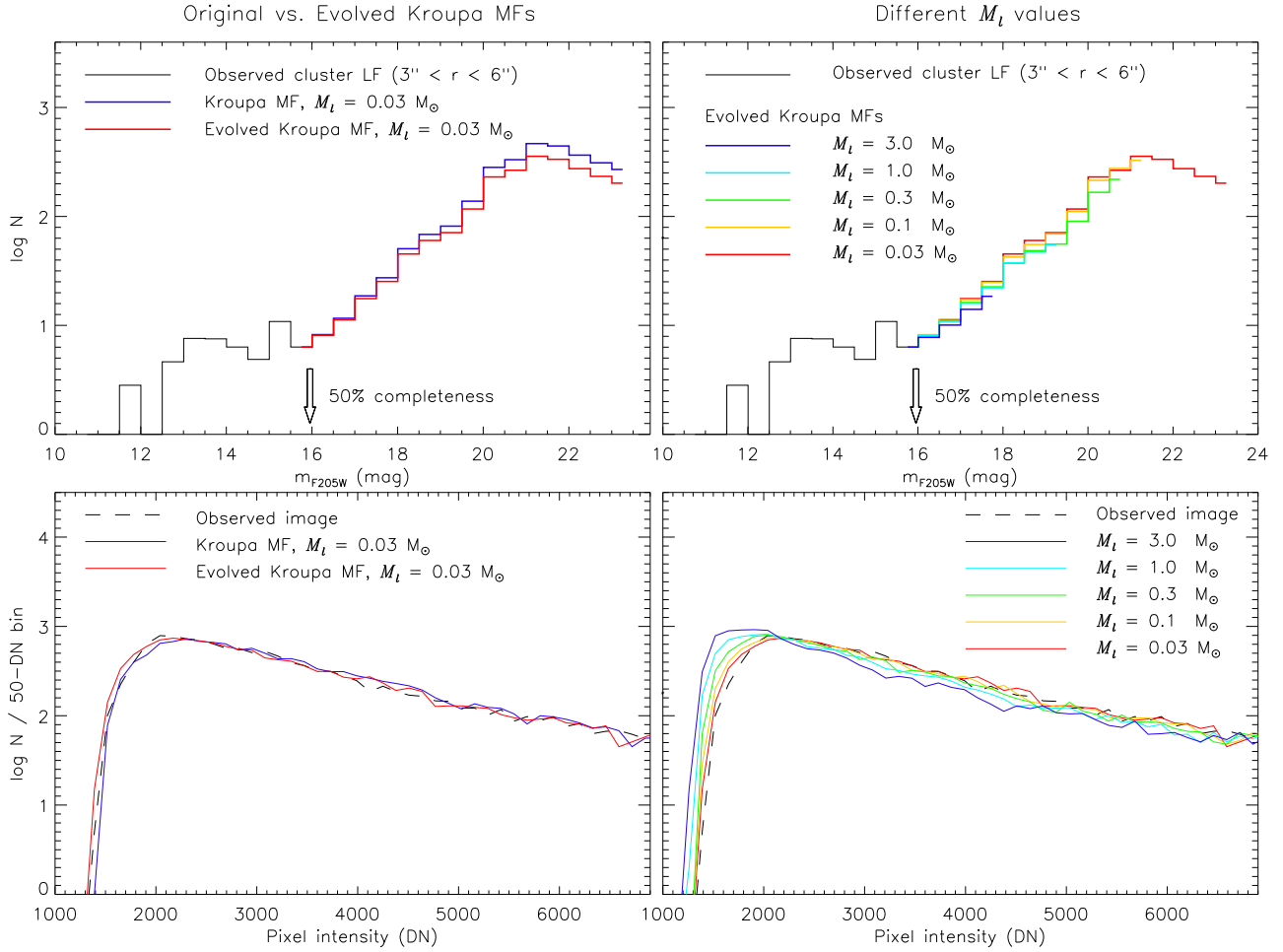


**Figure 8.** LFs and PIHs of the cluster field ( $3'' < r < 6''$ ) for the original Kroupa MF and the evolved Kroupa MF at 2 Myr (left panels) and for the five different  $M_i$  values for the evolved Kroupa MF (right panels).

of Kim, Morris & Lee (1999) and Kim et al. (2000). The Kroupa MF consists of three power-laws,  $\alpha = 2.3$  for  $M > 0.5 M_\odot$ ,  $\alpha = 1.3$  for  $0.08 < M/M_\odot < 0.5$ , and  $\alpha = 0.3$  for  $M < 0.08 M_\odot$ . Following Kim, Morris & Lee (1999), we adopted the following for the initial conditions of the F-P calculation: density and velocity dispersion structures from the King model, total mass of  $2 \times 10^4 M_\odot$ , upper mass boundary of  $150 M_\odot$ , tidal radius of 1.1 pc, and the King concentration parameter of 4.

Figure 7 shows the Kroupa IMF with  $M_i = 0.03 M_\odot$  and its evolved MF at 2 Myr from our F-P calculation for the two cluster annuli. The MF at 2 Myr is slightly steeper in the inner annulus, while it is slightly shallower in the outer annulus due to the mass segregation.

The synthetic LFs are constructed in the same way as in §4.1: the observed LF is adopted for the bright-part, and the faint-part LF is converted from the model MF and joined to the bright-part LF at  $m_{50}$ . The artificial images are then created in the manner described in §4.1.

The synthetic LFs and PIHs from the artificial images for the inner cluster annulus are shown in the left panels of Figure 8 for the two model MFs: the Kroupa IMF and its evolved MF. The difference in PIHs between the two model MFs are insignificant because the evolution of the MF is not

considerable for the first 2 Myr in the radial ranges of our consideration, as seen in Figure 7.

The right panels of Figure 8 compare the LFs and PIHs for the five evolved MFs with  $M_i$  values between  $0.03 M_\odot$  and  $3 M_\odot$ . The faint-part slopes of the LFs differ slightly for the different  $M_i$  values because the degree of mass segregation depends on  $M_i$ . Among the five PIHs, the one for  $M_i = 0.03 M_\odot$  best fits the observed PIH. MF models with  $M_i \gtrsim 0.3 M_\odot$  considerably underestimate the PIH.

Figure 9 plots the profiles of the  $S$  values as a function of  $M_i$  for the inner and outer annuli as well as the summed  $S$  profile for the two annuli. The minimum  $S$  values are found at  $0.03 M_\odot$  for the inner annulus and  $0.3 M_\odot$  for the outer annulus. When the two annuli are considered simultaneously, the minimum  $S$  is found at  $0.1 M_\odot$ . This clearly shows that a significant number of stars below  $1 M_\odot$  are required to match the observed PIH of the Arches cluster.

## 4 SUMMARY

In the present paper, we described a novel photometric method that compares PIHs between an observed image and artificial images constructed with various synthetic LFs to

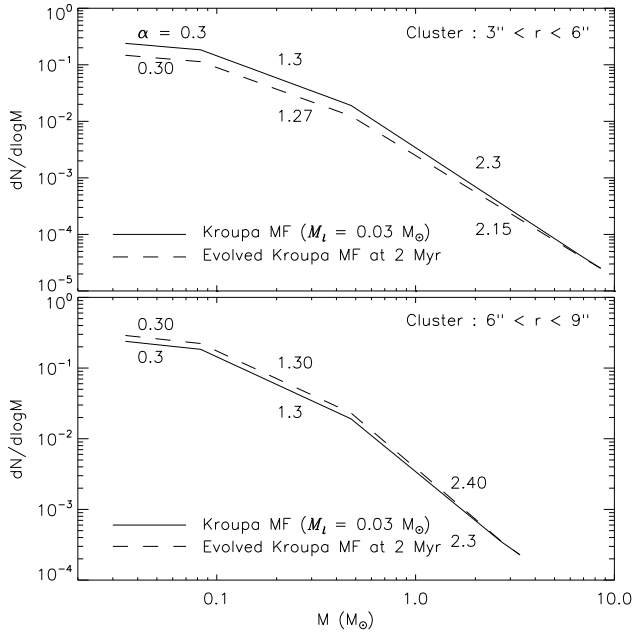


**Figure 7.** Original Kroupa MF (solid lines) and the dynamically evolved Kroupa MF at 2 Myr calculated using the Fokker-Planck model (dashed lines) below the masses that correspond to  $M_{50}$  for annuli of  $3'' < r < 6''$  (upper panel) and  $6'' < r < 9''$  (lower panel). The heights of the two MFs are adjusted to match at  $M_{50}$ .

estimate the shape of the low-end MF for the Arches cluster. The synthetic LFs were constructed by combining the observed LF above  $m_{50}$  and a model LF below  $m_{50}$ , which was converted from two different types of model MFs: single power-law MFs with various  $\alpha$  and  $M_l$  and the Kroupa MFs with various  $M_l$ .

In the case of the single power-law MF, we found the best-fits between the observed and artificial PIHs at ( $\alpha = 2.3$ ,  $M_l = 0.2 M_\odot$ ) for the inner annulus of  $3'' < r < 6''$  and at ( $\alpha = 1.9$ ,  $M_l = 0.02 M_\odot$ ) for the outer annulus of  $6'' < r < 9''$ . When the inner and outer annuli are considered together, the best-fit  $\alpha$  and  $M_l$  values are 2.2 and  $0.1 M_\odot$ , respectively, which is very close to the Salpeter IMF.

As a more realistic IMF model, we adopted the Kroupa IMF (Kroupa 2001) and used its dynamically evolved MFs calculated with the Fokker-Planck method. The best-fits between the observed and artificial PIHs were found at  $M_l = 0.03 M_\odot$  for the inner annulus,  $M_l = 0.3 M_\odot$  for the outer annulus, and  $M_l = 0.1 M_\odot$  for both annuli. This shows that the Arches cluster has a significant number of stars that are not resolved by current IR telescopes and that the most likely IMF of the Arches cluster is not too different from the IMF found in the Galactic disk.

## ACKNOWLEDGMENTS

We thank Professor Myong Gyoon Lee for helpful discussions and comments. J.S. appreciates Seungkyung Oh for the help with the IRAF package. S.S.K's work was supported by the Mid-career Research Program (No. 2011-0016898) through the National Research Foundation (NRF) grant

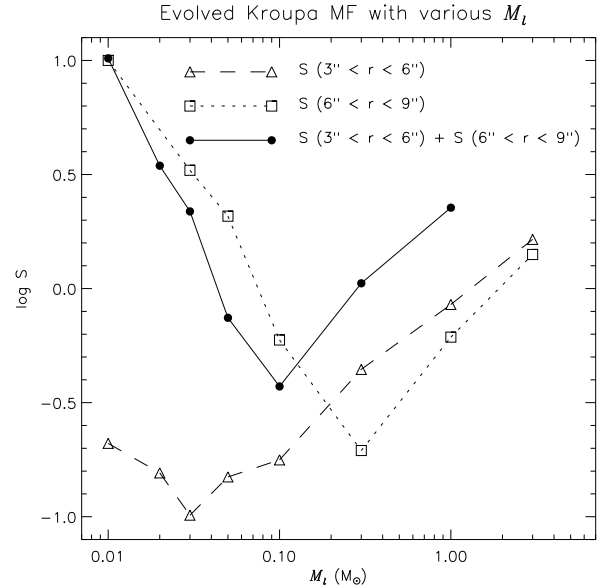


**Figure 9.**  $\log S$  values as functions of  $M_l$  for the evolved Kroupa MFs at 2 Myr. Triangles and squares are for the inner ( $3'' < r < 6''$ ) and outer ( $6'' < r < 9''$ ) annuli, respectively. Filled circles are for the two annuli together.

funded by the Ministry of Education, Science and Technology (MEST) of Korea.

## REFERENCES

- Espinoza, P., Selman, F. J., & Melnick, J. 2009, *A&A*, 501,563
- Figer, D. F., Kim, S. S., Morris, M., Serabyn, E., Rich, M., & Mclean, I. S. 1999, *ApJ*, 525, 750
- Figer, D. F., Najarro, F., Gilmore, D., Morris, M., Kim, S. S., Serabyn, E., McLean, I. S., Gilbert, A. M., Graham, J. R., Larkin, J. E., Levenson, N. A., & Teplitz, H. I. 2002, *ApJ*, 581, 258
- Kim, S. S., Figer, D. F., Lee, H. M., & Morris, M. 2000, *ApJ*, 545, 301
- Kim, S. S., Figer, D. F., Kudritzki, R. P., & Najarro, F. 2006, *ApJ*, 653, L113
- Kim, S. S., Morris, M., & Lee, H. M. 1999, *ApJ*, 525, 228
- Kroupa, P. 2001, *MNRAS*, 322, 231
- Lejeune, T., & Schaerer, D. 2001, *A&A*, 366, 538
- Martins, F., Hillier, D. J., Paumard, T., Eisenhauer, F., Ott, T., & Genzel, R. 2008, *A&A*, 478, 219
- Morris, M. 1993, *ApJ*, 408, 496
- Najarro, F., Figer, D. F., Hillier, D. J., & Kudritzki, R. P. 2004, *ApJ*, 611, L105
- Ortiz, R. & Lépine, J. R. D. 1993, *A&A*, 279, 90
- Polido, P., Jablonski, F., & Lépine, J. R. D. 2013, *ApJ*, 778, 32
- Reid, M. J. 1993, *A&A*, 31, 345
- Rieke, G. H., Rieke, M. J., & Paul, A. E. 1989, *ApJ*, 336, 752
- Salpeter, E. E. 1955, *AJ*, 121, 161
- Skrutskie, M. F. et al. 2006, *AJ*, 131, 1163



- Stetson, P. B., Hesser, J. E., Smith, G. H., Vandenberg, D. A., & Bolte, M. 1987, *AJ*, 97, 1360
- Stolte, A., Grebel, E. K., Brandner, W., & Figer, D. F. 2002, *A&A*, 394, 459
- Stolte, A., Brandner, W., Grebel, E., Lenzen, R., & Lagrange, A. 2005, *ApJ*, 628, L113
- Wainscoat, R. J., Cohen, M., Volk, K., Walker, H. J., & Schwartz, D. E. 1992, *ApJS*, 83, 111